Physics of Fluids ARTICLE pubs.aip.org/aip/pof

Dynamics of electrochemical dendritic propagation in circular domains

Cite as: Phys. Fluids **37**, 013347 (2025); doi: 10.1063/5.0246646
Submitted: 8 November 2024 · Accepted: 20 December 2024 ·
Published Online: 10 January 2025

Asghar Aryanfar,[1,a] Trina Dhara,[2,3] and Sunando DasGupta[2]

AFFILIATIONS

[1]Boğaziçi University, Bebek, Istanbul 34342, Turkey
[2]Indian Institute of Technology Kharagpur, Kharagpur, West Bengal 721302, India
[3]Cornell University, 113 Ho Plaza, Ithaca, New York 14853, USA

[a]Author to whom correspondence should be addressed: aryanfar@caltech.edu

ABSTRACT

The accumulation pattern in the dendritic microstructures in rechargeable batteries has a deterministic impact on their state of health and longevity. The dendrites either can cause early short-circuits or form dead lithium crystals during the prolonged charge–discharge cycles. We perform experiments, combined with percolation-based computations in parallel, to anticipate the dynamics in the state and rate of propagation of dendritic microstructures, in a circular domain. Subsequently, we develop a physical paradigm to correlate and verify the non-linear behavior in the growth dynamics. Coupling two approaches, we elaborate further on the location of the minimum growth rate, anticipate the main drive factor for microstructures, and get an estimation for the atomic-scale porosity. Additionally, we elaborate further on the role of curvature and the inter-electrode gap in enhancing/deviating from the typical Cottrell behavior. The established framework could be useful for designing the space of parameters for cell geometry, the electrolyte, as well as the charging condition to optimize for healthy operation and avoiding short-circuit.

I. INTRODUCTION

The surge of the energy demand is the consequence of the industrial development catalyzed by the widespread use of electric appliances.[1] Specifically, in the modern information age, the advancement of semiconductor and computing technology have been empowered by rechargeable batteries. In this regard, lithium-ion-batteries (LIBs) have been the flagship since 1991 and have fueled the extensive use in personal electronics, electric transportation, etc. However, the proliferation of vehicle electrification technology demands a prolonged charging time bottleneck to tackle, such that it equally competes with the internal combustion engine vehicle (ICEV) refueling timescale.[2,3] Building the fast charging infrastructure introduces the crux of scientific and engineering challenges associated with LIBs in terms of acquiring the time-effective energy density.[4–7]

The recent proposition of the high energy density lithium metal anode has shown to be satisfactory for the replacement of the conventional graphite anode. However, its propensity for dendritic growth during the charging phase remains a critical concern.[8] The unrestrained growing front may penetrate the separator material and connect the other electrode leading to catastrophic short-circuiting.[9,10] Additionally, the broken part of dendrites being completely covered by the insulating solid electrolyte interface (SEI) may accumulate on the electrode surface to form dead lithium which escalates the internal resistance, leading to the Columbic loss and thermal degradation. Such sequence of events ultimately damages the battery and causes the electrochemical degradation.[11,12]

In fact, dendritic growth has allured curious minds earlier than the batteries (LIBs), as electroplating had been utilized during the coatings for corrosion resistance and mechanical strength of metal finished products.[13–15] As a result, the morphology and grain size of the electrodeposited micro-structures have already been paramount to obtain the desired coating characteristics.[16,17] Meanwhile, these three dimensional growing structures (i.e., naming dendrites) have been visualized for a number of metals, such as zinc Zn, copper Cu, and silver Ag.[18,19] Experiment-wise, several studies have been employed to mitigate and control the dendritic morphology, which can be broadly classified into three categories of materials/electrolyte modulation, interface engineering, and bulk engineering. In this regard, the prior research has explored the role of the current density,[20] electrolyte composition,[21,22] surface defects (i.e., kinks),[23] interaction with the solid electrolyte interphase (*SEI*),[24,25] shielding with alternative compounds,[26] imposing external magnetic fields,[27] additives,[28] temperature,[29,30] self-healing

electrostatic shield,[31] separator design,[32–34] and 3D porous current collectors.[35,36]

Modeling-wise, earlier frameworks for the formation of the dendritic structures focused on space charge region and the strength of the electric field as the governing factors.[37] Later on, the effect of the ionic concentration was adopted as the drive for their evolution, particularly during the diffusion-limited aggregation regime (*DLA*),[38–42] where the root cause and mechanism were analyzed for the formation of tree-like structures.[43] Further modeling works on the dendritic formation include exploring the role of suppressing arrays,[44] guiding scaffolds,[45] surface roughness,[46] and leading to consequential instability.[47]

Contextually, substantial efforts have been probed to understand the shape of the concentration boundary layer around the disc-shaped aggregates and the morphological aspects of during radial growth pattern.[48,49] In this regard, particularly, the transition from fractal to dense morphology has been intriguing which can be controlled vs the applied potential, electrolyte concentration, and curvature[50–52] and can additionally be characterized vs fractal dimension.[51,53] Furthermore, the morphology distinction has been established in both diffusion- and migration-controlled regimes,[54] and its stability has been explored beyond the limiting current.[55] However, none of the previous works addressed the kinetics of the radial development in the microstructures.

In this paper, we explore the behavior in the microstructure growth rate (i.e., velocity) in the radial domain, both experimentally and computationally. We establish a percolation-based framework for computing the radial properties of the dendrites, and we discern a fast-slow-fast behavior in the growth regimes, which is addressed vs the deterministic factors for the growing of the microstructures. The obtained framework could be useful for optimizing the space of parameters for designing rechargeable batteries with the curved electrodes.

II. EXPERIMENTAL

The experiments were carried out within an established circular domain of an electrochemical cell, as shown in Fig. 1. An insulated copper wire (AWG 28, $\rho = 0.2\,\Omega\,\mathrm{m}^{-1}$, $d = 0.321$ mm) was purchased from Khaitan Winding Wire Pvt. Ltd. (KWW Wires and Strips), the surface was polished with sand paper of grit 200 and was bent into a circular shape ($d_0 = 18$ mm). Subsequently, it was placed on a microscopic glass slide, purchased from HiMedia Laboratories Pvt. Ltd. to be used as the anode. For the cathode, the tip of a copper wire (AWG 32, $\rho = 0.5\,\Omega\,\mathrm{m}^{-1}$, $d = 0.202$ mm) was purchased from KWW Wires and Strips and was fixed manually at the center of the circular anode. The circular domain is filled with the electrolyte solution slowly drop by drop using a micropipette, which is a specified concentration of copper sulfate salt ($CuSO_4.5H_2O$, EMPLURA 99%) in de-ionized water (Milli-Q, 99.8%) as the solution. The ends of the electrodes were connected to the power source (KEITHLEY 2410 1100 V source-meter), and the array of the specified voltage V_0 was applied in separate experiments. A camera with macro-lens (M2101K6P, 1944 × 2592 pixels, focal length: 4 mm, and exposure time: $\frac{1}{50}$ s) is fixed below the glass slide to capture the dendritic growth from the bottom. Table I summarizes the experimental details.

Throughout each experiment, the image acquisition was taken in the assigned rates, which includes every 20 s for the faster growth and every 40 s for the slower developments. Hence the image acquisition rates varied from 1frame/40 s to 1frame/20 s. Figures 2(a) and 2(b) illustrate two image-samples with different morphologies. The microstructures initiate from the inner electrode (i.e., d_I) and progressively propagate toward the counter-electrode (i.e., d_O).

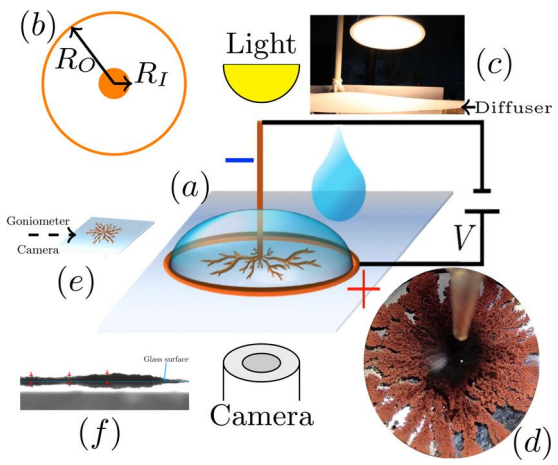

FIG. 1. Experimental setup for microstructure observation/tracking. (a) Three dimensional view of the electrolyte drop on the glass slide, with the electrode connected to + and − poles. (b) The cross-sectional view of the negative electrode (wire cross section) in the center and the ring positive electrode in the periphery, with the radii of R_I and R_O, respectively. (c) Light source diffused through a white paper. (d) Sample top view of the grown electrodeposits. (e) Post-experiment measurement method of the microstructure thickness, from the lateral view, using a goniometer. (f) Sample thickness measurements from different positions of the microstructure.

For capturing the side view of the disc-shaped electrodeposits and their average thickness $\bar{b}$, the electrolyte was absorbed with blotting paper carefully after experiment, where in most cases the structure had minimal damage and remained almost intact. Afterward, the ring electrode was removed, followed by the detachment of the central electrode. The remaining electrodeposits on the glass slide [Fig. 1(e)] were aligned from the side view to the goniometer camera (Dataphysics OCA 15Pro), and the image for thickness measurement was captured [Fig. 1(f)]. Hence, the average gross thickness of the deposits $\bar{b} \approx 30\mu$m was obtained.

III. COMPUTATIONAL

The experimentally captured microstructures were identified with the highest possible accuracy and computationally analyzed after. The image processing procedure for capturing the microstructures has been itemized as below:

TABLE I. Experimental parameters. The electrodes are copper *Cu* and the electrolyte is aqueous copper sulfate $CuSO_4$ solution (i.e., C_0).

d_I(mm)	d_O(mm)	V_0(V)	C_0(mM)	Image acquisition rates (frame/s)
0.2	18	$\{3, 4, 5, 6, 7\}$	$\{5, 10, 25\}$	$\left\{\frac{1}{20}, \frac{1}{30}, \frac{1}{40}\right\}$

(a) Branched morphology formation for $(C_0, V_0) = (10mM, 3V)$ at $t = 500s$.

(b) Packed morphology formation for $(C_0, V_0) = (10mM, 5V)$ at $t = 180s$.

FIG. 2. The variation in the observed morphology of the electrodeposits.

1. Each image *Im* has been read into the three distinct red, green, and blue matrix distributions $\{R, G, B\} \in [0, 255]$. Subsequently, it has been converted to the gray-scale image I by using the appropriate proportions f of each color, defined as[56]

$$f = [0.299 \quad 0.587 \quad 0.114], \tag{1}$$

which leads to

$$Int = \frac{1}{255}(f_1 R + f_2 G + f_3 B). \tag{2}$$

Then, the obtained gray-scale image is normalized to the maximum value to achieve the intensity value of: $Int_{i,j} \in [0, 1]$.

2. The gay-scale image $Int_{i,j}$ is binarized using global thresholding value that was originally introduced by Otsu.[57] Hence, the threshold value Int_c determines if a given pixel will be turned to black (i.e., 0) or white (i.e., 1), as follows:[58]

$$J_{i,j} = \begin{cases} 1 & Int_{i,j} \geq Int_c \\ 0 & Int_{i,j} < Int_c. \end{cases} \tag{3}$$

Such local grayness threshold is attained via the minimization of the weighted intra-class variance σ^2,[59] defined proportionally as follows

$$\begin{cases} \sigma^2 = \omega_0 \sigma_0^2 + \omega_1 \sigma_1^2 \\ \omega_0 + \omega_1 = 1, \end{cases} \tag{4}$$

where ω_0 and ω_1 are the individual weight of each black (0) and white (1) portions as the fraction of total, and σ_0^2 and σ_1^2 are their respective variances. Such minimization ensures that the resulting black and white groups are selected from the most similar numbers in the closest proximity of each other (i.e., closest ∼lowest variance). Hence, the obtained black and white (i.e., binary) image is the best approximation from the original gray-scale image, and the optimization of the threshold for obtaining the critical value Int_c ensures that the microstructure borders are the most discernible compared to those obtained from the other threshold values.

3. The center pixel of the image (i.e., average of the boundary points) was taken as the initial seed. Starting from this point and percolating through the first order neighbors (left ←, right →, top ↑, and bottom ↓), the region of the dendritic structure is captured until reaching the boundary of the microstructure, where no further progress is possible.
4. Extracting the microstructure from the previous step, a more accurate center location was redefined by averaging its horizontal and vertical extents.
5. Starting from the real center, obtained in the previous step, as the seed point, the percolation through first-order neighbors (left ←, right →, top ↑, and bottom ↓) was repeated, until reaching to the extents of the microstructure, where no further progress is possible. Throughout the percolation, each pixel is indexed from the higher to the lower value, based on the number of the iteration it has been captured. Hence, the index of each pixel is correlated by its distance from the center (i.e., seed) location. Figure 3 (a) illustrates a sample of such percolating cluster.

As the electrodeposits stochastically develop in highly branched form, we characterized their distinct radial properties defined below.

The reach of the microstructure represents the extent of the inter-electrode domain toward the counter-electrode. As this relates to the outer peripheral regions, the convex hull of the propagating cluster is a suitable measure [dashed line in Fig. 3(a)], which has been illustrated in Fig. 3(b) (i.e., orange dashed circle and solid vector) for a sample microstructure. Hence, being the inner R_I and outer R_O radii, one has $R_I \leq \text{Reach} \leq \text{R}_\text{O}$, and normalizing to the outer radius R_O,we get

$$\approx 0 < \hat{r} \leq 1, \tag{5}$$

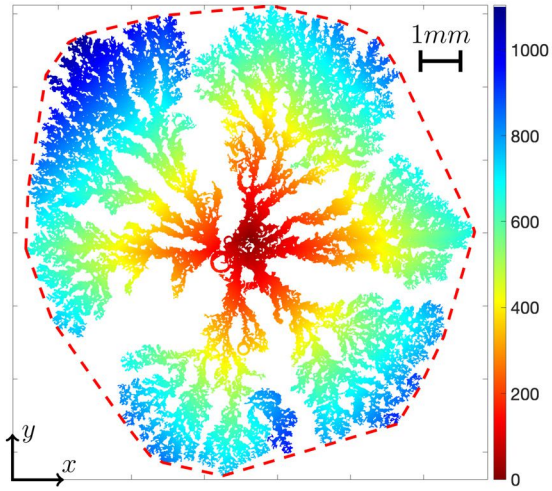

(a) The center-initiated percolation from the center of a microstructure produced at concentration and voltage of $\{C_0, V_0\} = \{5mM, 5V\}$, where the color commensurate with the propagation step. Red dashed lines: the convex hull enclosing the formed microstructure, used as a measure for calculating the reach $\hat{r}$.

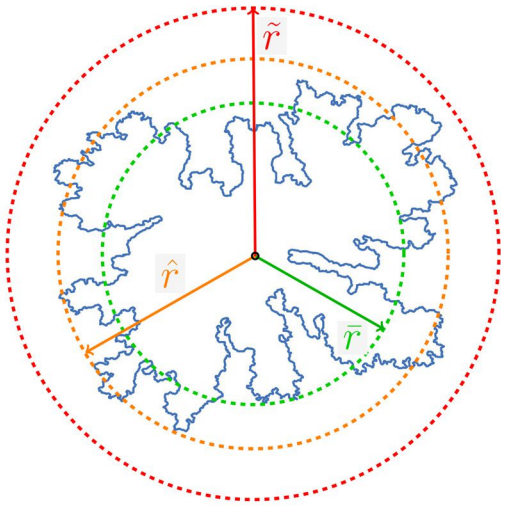

(b) Characterization of radial measures for the evolving microstructure sample: $\bar{r}$: the average radius, representing the macro-scale solid material, $\hat{r}$: The reach of the micro-structure, obtained from the convex hull, $\tilde{r}$: The effective radius of the microstructure, containing the identical periphery as the real state for electrodeposition.

FIG. 3. (a) Percolation-based image processing for the microstructures and (b) radial characterizations.

where the approximation sign is used since $R_I \ll R_O$. Mathematically the reach $\hat{r}$ can be calculated from the following equation:

$$\hat{r} = \frac{\beta}{N_{\mathrm{CVX}} R_O} \sum \sqrt{(x_{\mathrm{CVX},i} - x_C)^2 + (y_{\mathrm{CVX},i} - y_C)^2}, \tag{6}$$

where β is the calibration factor, converting a pixel to the real dimension $[\beta] = m/\mathrm{Pixel}$, N_{CVX} is the number of points in the convex hull [$N_{\mathrm{CVX}} = 13$ in Fig. 3(a)], $x_{\mathrm{CVX},i}, y_{\mathrm{CVX},i}$ are their horizontal and vertical coordinates and x_C, y_C are the horizontal and vertical coordinates of the center.

The average radius $\bar{r}$ is the radius of the circle with the equivalent solid area as of the microstructure. Hence,

$$\bar{r} = \frac{\beta}{R_O} \sqrt{\frac{N}{\pi}}, \tag{7}$$

where $N = \sum_{i=1}^{N} 1$ sums up the entire pixels recognized as part of the microstructure. $\sum 1 = \pi \bar{r}^2$).

The equivalent radius $\tilde{r}$ is the radius of a circle having identical peripheral length as of the periphery of the microstructure. Hence, it is defined as follows:

$$\tilde{r} = \frac{\beta}{2\pi R_O} \sum_{j=1}^{N_p} \sqrt{(x_{j+1} - x_j)^2 + (y_{j+1} - y_j)^2}, \tag{8}$$

where N_p is the number of points constituting the periphery of the microstructure, and the index j is the label of its successive points.

Figure 3(b) illustrates the reach $\hat{r}$, average radius $\bar{r}$ and the equivalent radius $\tilde{r}$ for a sample microstructure, where one generally has

$$\bar{r} \le \hat{r} \le \tilde{r}, \tag{9}$$

where the equality occurs for a perfect circle, and the values diverge as a function of the included voids (porosity) and branches. Having these measures, the dynamics of the propagating electrodeposits has been explained next. In this regard, performing computations, Fig. 4(a) shows the evolution of reach $\tilde{r}$ in time t for different voltage values and Figure 4(b) shows the short-circuit time t_S versus applied voltage V for various concentrations C0.

A. Velocity

The extent of the progress of the microstructure can effectively be recognized from the reach $\hat{r}$, which eventually leads to the short-circuit. In this regard, the growth velocity $v(t_k)$ of the electrodeposits in the given time t_k can get calculated as

$$\hat{v}(t_k) = \frac{\hat{r}(t_{k+1}) - \hat{r}(t_k)}{\delta t}, \tag{10}$$

where $\delta t = t_{k+1} - t_k$ and $\hat{v}$ is the normalized velocity to the outer radius R_O. Figures 5(a)–5(c) illustrate the computed experimental rate of propagation $\hat{v}$ vs the extent of the microstructure progress $\hat{r}$ for the ranges of applied voltage V_0 and the electrolyte concentrations C_0 given in the Table I. The dashed lines show the interpolation curves, the form of which is explained later in the paper.

$$\hat{v}_{\mathrm{FIT}} = \frac{1}{a_1 \hat{r} R_O \left(\ln(R_O) - a_2 \ln(\hat{r} R_O)\right)}. \tag{11}$$

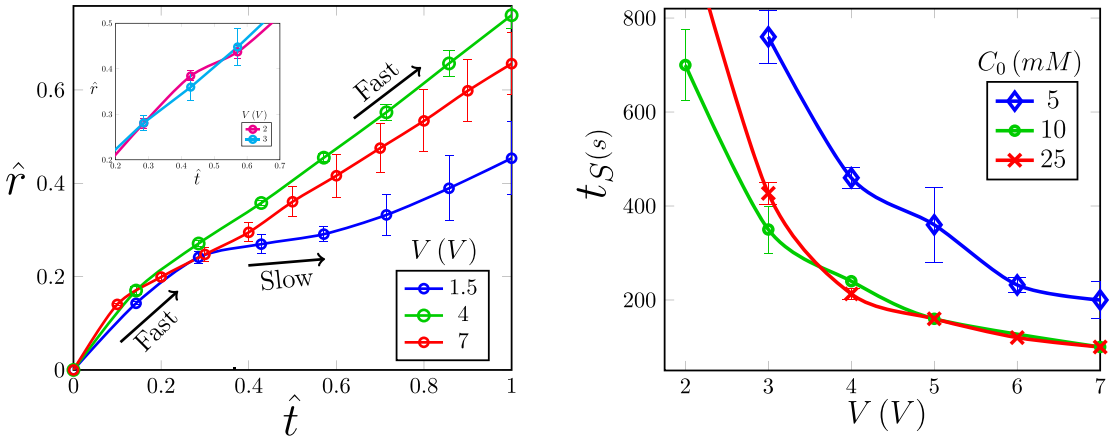

(a) The average computed normalized reach $\hat{r}$ of the microstructures versus the normalized time $\hat{t}$, illustrating the inflection points. The standard deviations are shown as error bars.

(b) Short-circuiting time t_S versus the applied voltage V and the electrolyte concentration C_0.

FIG. 4. Visualization of experimental data.

The derivation for the form of interpolating fitting function $\hat{v}_{\mathrm{FIT}}$ has been described later in Sec. IV.

B. Diffusivity

The time-dependent measurement of the progress of the microstructure allows to compute the rate of ionic feeding into the electrodeposits, which correlates directly with the total running current I. In fact, due to the three-dimensional nature of the growing structure, the current is consumed on both inner bulk B, normal to the plane of propagation, as well as outer (peripheral) surface S regions, in the propagation plane. In other words, while the former thickens the microstructure, the latter extends the radial propagation. Hence, one has

$$I = 2I_B + I_S, \tag{12}$$

where I_B and I_S are the currents consumed in the inner bulk and outer surface (i.e., peripheral) sites, respectively, and the coefficient of 2 is used since both the top and bottom of the microstructure are the ionic-feeding sites from the electrolyte. In fact, more detailed explanation of the current transition in time is given via the Cottrell relationship, which in circular domain with cylindrical shape, turns into[60]

$$I \approx 2nFA_BD_{\mathrm{INT}}C_0\left[\frac{1}{\sqrt{\pi D_{\mathrm{APP}}t}}\right] + nFA_SD_{\mathrm{INT}}C_0\left[\frac{1}{\sqrt{\pi D_{\mathrm{INT}}t}} + \frac{1}{2\bar{r}}\right], \tag{13}$$

where n is the valence number of the charge carriers, F is the Faraday's constant ($96.5\mathrm{kCmol}^{-1}$), C_0 is the concentration of ambient electrolyte, t is the time, A_B and A_S are the apparent surface area of the microstructure ($A_B \approx \pi\bar{r}^2$), normal to the direction of the propagation and

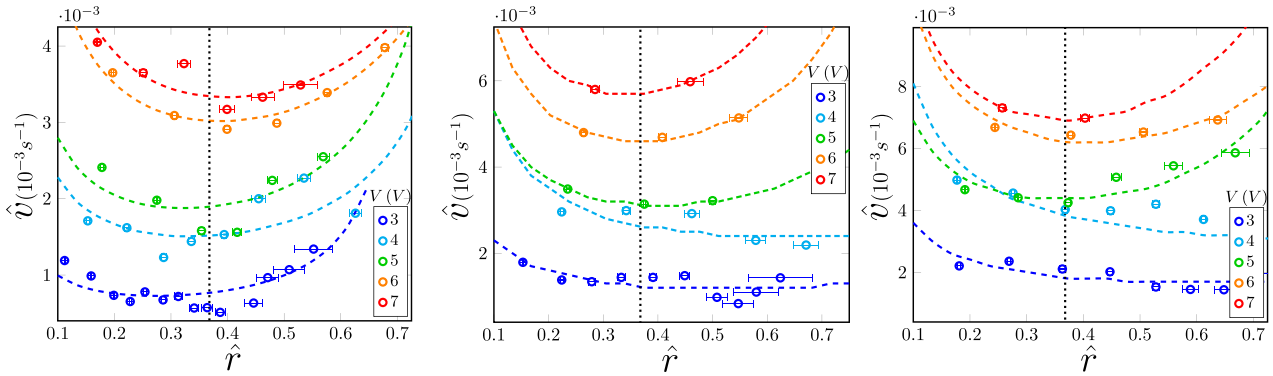

(a) $5mM$ (b) $10mM$ (c) $25mM$

FIG. 5. Computed rate of growth in the normalized velocity $\hat{v}$ vs the extend of the microstructure progress $\hat{r}$ for the given range of voltages V_0 in different concentrations C_0. The dashed lines show the interpolation [later in Eq. (22)] and the dot line represents the location of minimum electric field at the progress scale of 37% [later obtained in Eq. (21)].

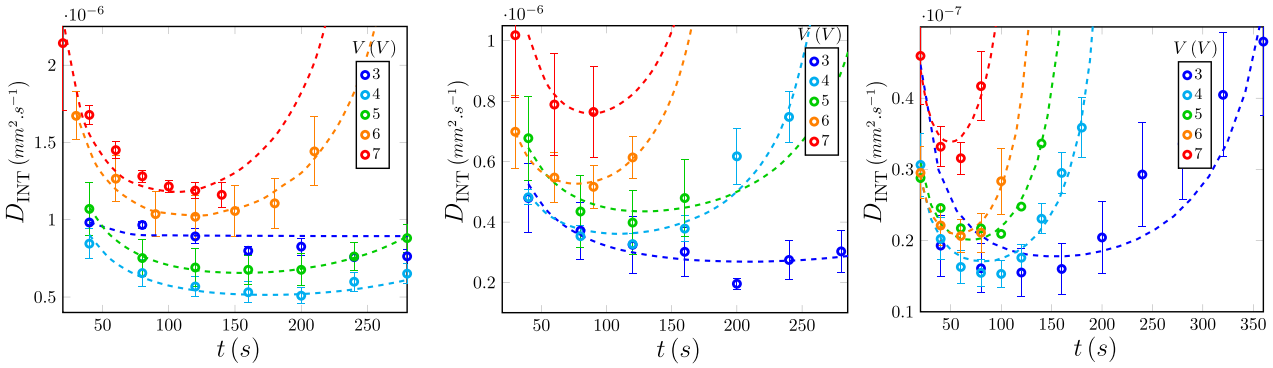

(a) $5mM$, Err $\approx 5.5\%$ (b) $10mM$,Err $\approx 5.5\%$ (c) $25mM$, Err $\approx 8.7\%$

FIG. 6. Computed interfacial diffusivity values D_{INT} vs time t for the given range of voltages V in different concentrations C_0. Scatter points: Experimental data, followed by computational processing and dashed lines: the curve-fitting interpolations.

apparent peripheral area ($A_S \approx 2\pi\tilde{r}\bar{b}$ and $\bar{b}$ is the average thickness and $\tilde{r}$ is the equivalent radius) in the direction of propagation. The notion of the interfacial diffusivity here is to distinguish it from the typical diffusivity D values of ion in a bulk solution in the absence of the porous microstructure. In fact, calculating the interfacial diffusivity D_{INT} in the presence of the microstructure later on will shed light into estimating their porosity ϕ.

From the transient Cottrell Eq. (13), one could calculate the transient in the interfacial diffusivity D_{INT} during the growth of the microstructure, which is fairly different than the reported bulk value D of the electrolyte in the absence of the microstructure. Calling the charge per volume $q = nFC_0$, it can be simplified into a quadratic form of $\sqrt{D_{\mathrm{INT}}}$ as

$$Q_1 D_{\mathrm{INT}} + Q_2\sqrt{D_{\mathrm{INT}}} + Q_3 = 0, \tag{14}$$

where Q_1, Q_2, and Q_3 are the coefficients obtained as follows:

$$\begin{cases} Q_1 = \dfrac{qA_S}{2\tilde{r}}, \\ Q_2 = \dfrac{q(2A_B + A_S)}{\sqrt{\pi t}}, \\ Q_3 = -I, \end{cases} \tag{15}$$

where the solution the transient interfacial diffusion coefficient D_{INT} is obtained as

$$D_{\mathrm{INT}} \approx \frac{\tilde{r}^2}{A_S^2}\left(\sqrt{\frac{(2A_B + A_S)^2}{\pi t} + \frac{2A_S I}{q\tilde{r}}} - \frac{(2A_B + A_S)}{\sqrt{\pi t}}\right)^2. \tag{16}$$

Figures 6(a)–6(c) present the transition of the computed interfacial diffusivity D_{INT} for the given range of voltages V_0 in different concentrations C_0. The dashed lines show the interpolation curves, the function form of which is elaborated on, later in Eq. (22). In the mean time, the mismatch measure Err of the fitting diffusivity values D_{FIT} (dashed lines) with the calculated interfacial diffusivity values from the experiments D_{INT} (points with error bars) could get derived as

$$\mathrm{Err} = \frac{1}{N}\sum_{i=1}^{N}\left|\frac{D_{\mathrm{FIT},i} - D_{\mathrm{INT},i}}{D_{\mathrm{INT},i}}\right|, \tag{17}$$

where N is the number of the measurements for each experiment. The average of the mismatch measure Err for each concentration C_0 and its set of voltage values V is noted in the respective caption.

IV. RESULTS AND DISCUSSIONS

A. Role of electric field

The experimental measurement for the progress of the diffusion front $\hat{r}$ as a function of time t in Fig. 4(a), shows a *fast-slow-fast* behavior, which is later illustrated in terms of the speed of the development $\hat{v}$ in Figs. 5(a)–5(c), with a positive curvature (curving-up) trend. The root cause of this behavior could be inherited from the electric field E, which is obtained from the voltage distribution (i.e., $E = -\nabla V$). The voltage distribution per se can be obtained via solving the Gauss relationship (i.e., $\nabla^2 V = -\frac{\rho}{\epsilon}$). In this regard, the polar coordinates (r, θ) would be the most appropriate for the propagation domain geometry in Figs. 2(a) and 2(b). Assuming electro-neutrality in the substantial bulk space of the inter-electrode medium of the fast-growing electrodeposits, the Gauss relationship gets simplified into $\frac{d}{dr}\left(r\frac{dV}{dr}\right) \approx 0$. Considering the progress scale of the microstructure external boundary is s (i.e., $s = \hat{r}R_O$), one can solve it with the respective potentiostatic boundary condition of $V(s) = V_I$, $V(R_O) = V_O$ as

$$V(r) = V_- + \left(\frac{\ln(r) - \ln(s)}{\ln(R_O) - \ln(s)}\right)\Delta V, \tag{18}$$

where $s \le r \le R_O$. Respectively, the electric field E will be solely in the radial direction, merely due to azimuthal symmetry, and will be obtained as

$$E = \left.\frac{\partial V}{\partial r}\right|_s = \frac{\Delta V}{s\ln\left(\frac{R_O}{s}\right)}. \tag{19}$$

The obtained electric field shows an opposing behavior where $E \sim \frac{1}{s}$, shows faster growth in the earlier stage of development ($s \to 0$) while $E \sim \frac{1}{\ln\left(\frac{R_O}{s}\right)}$ indicates the faster speed of development at the later

stages (i.e., $s \to R_O$). Hence, there must be a minimum position in between s_{min} leading to the minimum electric field E_{min}, and it can be obtained by setting $\frac{\partial E}{\partial s} = 0$, which gives

$$\frac{\partial E}{\partial s} = \frac{1}{\ln(R_O) - \ln(s)} \left(\frac{1}{\ln(R_O) - \ln(s)} - 1 \right) \frac{\Delta V}{s^2} = 0, \quad (20)$$

which requires $\ln\left(\frac{R_O}{s}\right) = 1$, and one gets

$$s_{min} = \frac{R_O}{e} \approx 0.37 R_O. \quad (21)$$

Figure 7 illustrates the electric field profiles for different applied voltage values, where the location of the minimum electric field E_{min} is highlighted. In fact, the initial slow-down and later speed-up behavior in the rate of microstructure growth $\hat{v}$ could get correlated with the local interfacial electric field. Hence, the interpolation of the speed of the growth $\hat{v}$ could get interpreted in the forms of fitting interpolation function f_{FIT}, similar to the form of electric field in Eq. (19), with the coefficients of relaxations a_1, a_2 as follows:

$$f_{\text{FIT}} = \frac{a_1}{s(\ln(R_O) - a_2 \ln(s))}. \quad (22)$$

Performing non-linear regression and error minimization, the interpolated forms of the growing velocity $\hat{v}$, for the most part, correlate visually with the experimental computations in Figs. 5(a)–5(c). In other words, the velocity trend $\hat{v}$ carries the footprint of the electric field E, with discernible location of minimum velocity v_{min} correlating with that of electric field $s_{min} = 0.37 R_O$.

The computed range of the interfacial diffusivity D_{INT} can open insights into the porosity of the growing microstructures. While the computed bulk A_B and peripheral A_S only consider the larger-scale pores, discernible with the naked eye with porosity ϕ_{Macro}, they do not account for the micro-/nano-scale porosity ϕ_{Micro}. In other words, the assumption of the fully occupied real-estate of the microstructure needs to be modified and the cavities, which include a significant fraction of their bodies, should be excluded. Hence, the real diffusivity D will be far less in magnitude. Assuming the inclusion of micro-pores in the bulk and surface of the microstructure, their corrected areas will be $(1 - \phi_{\text{Micro}})A_B$ and $(1 - \phi_{\text{Micro}})A_S$, respectively. Therefore, correlating with the diffusivity-area ($D \sim A$) in Eq. (16), the real diffusivity D gets related to the interfacial diffusivity D_{INT} as

$$D \approx (1 - \phi_{\text{Micro}}) D_{\text{INT}}, \quad (23)$$

and the approximation sign has been used for assuming the uniform porosity across the entire microstructure. The experimental bulk diffusivity measurement for copper ion Cu^{2+} in copper sulfate $CuSO_4$ in the literature in the absence of applied voltage and reactions is in the range of $D \sim 10^{-10} \frac{m^2}{s}$.[61] One could compare the obtained interfacial diffusivity value $D_{\text{INT}} \sim 10^{-6} \frac{m^2}{s}$ [Figs. 6(a)–6(c)] with this range, noting that the former is electrochemical (fast, occurring in the interface) and the latter is physical (slow, occurring in the bulk), which leads to estimation of the micro-scale porosity ϕ_{Micro} as

$$\phi_{\text{Micro}} \sim 99\%, \quad (24)$$

which proves that the internal structure of the dendrites is significantly porous.

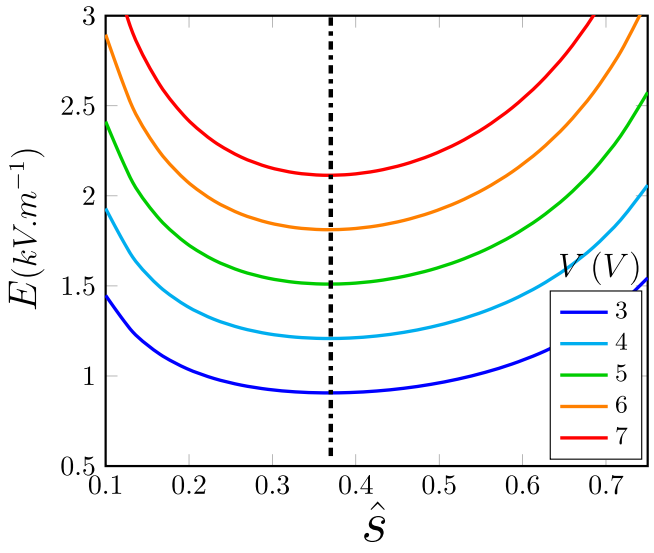

FIG. 7. The trend of electric field during the growth.

B. Enhanced Cottrell effect

A similar trend has been observed in the computed interfacial diffusivity D_{INT}. In this regard, the initial monotonous decrease in the current density I could get correlated with the Cottrell's conjecture on the local depletion of the existing ions. Hence, upon applying voltage, the ions migrate to the cathode and get reduced, and upon their exhaust, the other ions in the bulk will transport-in where their diffusion becomes a controlling factor. As well, the electric field contains the information curvature-induced augmentation of the electric field E_{Curved}. Hence, the augmentation ratio $f(s)$ could be obtained via comparing it vs the flat counterpart E_{Flat}, as follows:

$$f(s) = \frac{E_{\text{Curved}}}{E_{\text{Flat}}} = \frac{1}{s} \frac{R_O - s}{\ln(R_O) - \ln(s)}.$$

It is obvious that $\lim_{s \to 0} f(s) = \infty$, which is the sole effect of the curvature. In fact, during the initiation of the microstructures on the electrode with the smallest radius (i.e., highest curvature), the curvature-induced electric field is the highest which enhances the current I vs time t trend in the Cottrell relationship.

However, as the microstructures grow, as they are conducting as the cathode material, the inter-electrode gap is progressively reduced, which augments the electric field. During the significant propagation of electrodeposits, just before the short-circuit event, such electric field exponentially grows, and the ionic transportation becomes electromigration-controlled, which causes jump in the real-time current I and the computed interfacial diffusivity D_{INT}. This can be shown from Eq. (19), where during the last stages of the dendritic propagation, since $\lim_{s \to R_O} \frac{1}{\ln(R_O/s)} = \infty$, the imposed electric field causes the current jump, which is seen in Figs. 5(a)–5(c). In the meantime, the location of the minimum electric field $s_{min} = 0.37 R_O$ shows visual agreement with the minimum growth rate $\hat{v}_{min}$ in these figures. Additionally, while there is a direct correlation with the growth position $\hat{s}$ and the time t, the zone of such minimum is observed in the

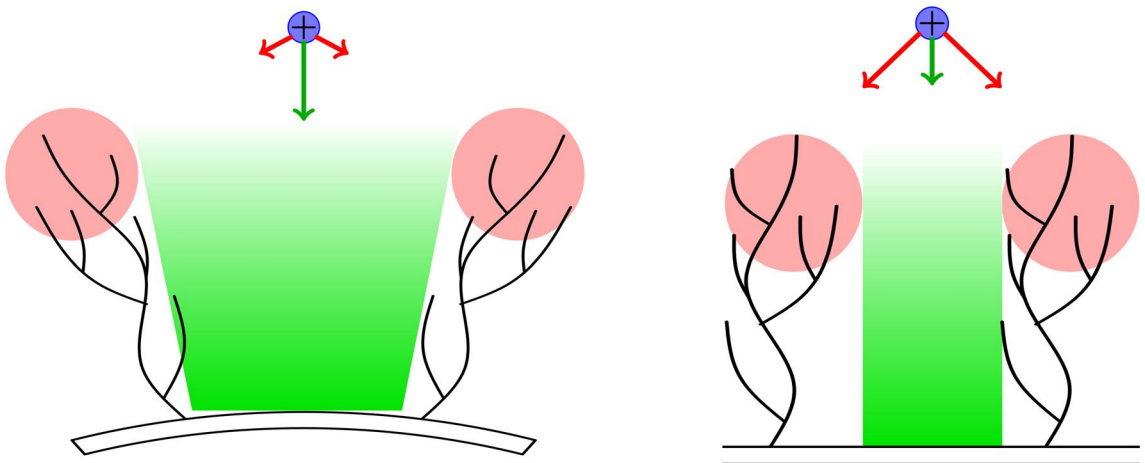

(a) Curved electrode geometry. (b) Flat electrode geometry.

FIG. 8. Schematics of the feasibility of the pathway for the electrodepositing ion (blue), when exposed to (a) curved vs the (b) planar geometry of the electrodes. The tendency of the movement is shown by the red and green vectors which are toward the peak of the dendrites (highlighted red) vs the inner regions (highlighted green). As shown, the curved geometry provides more openness for the formation of packed micro-structures. Reproduced with permission from Phys. Rev. E. 108, 014801, Copyright 2023 American Physical Society (APS).[62]

computed local interfacial diffusivity D_{INT} in Figs. 6(a)–6(c), showing the significance of the electric field in such a fast-propagating regime.

Needless to mention that the kinetics of the microstructure growth in this study in the circular domain differs from that of the planar electrode in the initial stages of growth, while later on, shares a similar dynamics in the final stage of development. Geometry-wise, during the instigation, the macro-scale real estate for planar electrode remains constant and the growth rate is roughly uniform, while for the curved surface, the very small initial real estate for the electrodeposition grows significantly per electrodeposition as it covers the electrode surface (i.e., $A = 2\pi r$, where A is the electrodeposition area and r is the reach). Hence, for the curved surface, the initial radius of electrodeposition gets enlarged significantly, which leads to decrease in the growth rate. Alternatively, one can think the dendrites grown on the circular geometry to have more opening than those of planar electrode, which reduces the growth rate. As illustrated in Fig. 8, while on the flat electrode, there is more possibility to attach to the peak of the electrodeposits (i.e., longer and more porous), on the curved electrode there is more opening and which provides more possibility to diffuse inside (i.e., shorter and more packed).

However, in the later stages of the electrodeposition, the remaining gap between the microstructure and the counter electrode will predominate over the surface curvature effect. The electric field will grow excessively and hence the dendrites in both planar and circular domains will similarly accelerate with a runaway behavior. Therefore, in total, considering both the geometry effect (initial stages) and gap effect (final stages), the dendrites grown on the planar electrode will grow faster than the circular counterpart, with all other conditions fixed (electrode gap, applied voltage, and electrolyte composition) and are more likely to cause short-circuit.[62]

V. CONCLUSIONS

In this paper, the non-linear kinetics of the dendritic growth on the circular domain has been investigated. The fast-slow-fast propagation pattern has been observed in the real-time experimental measurements, which has been analyzed via developing a percolation-based image processing protocol. Such, the kinetics has been complemented/verified via analytical derivation of effective parameters for electrochemical ionic flux, such as electric field and transient diffusivity, where the minimum pace of propagation and minimum magnitude of electric field are correlated at progress scale of 37% in the inter-electrode gap. The underlying reason for the fast kinetics in the early and late stages of the interface development have been addressed. In particular, we estimate the location of the minimum growth rate via spotting the minimum in the electric field. Finally, we comment on how to estimate the atomic-scale porosity of the growing microstructures, via comparison of the experimental and analytical derivations of the growth kinetics, where the dendrites turn out to be extremely porous ($\phi_{\mathrm{Micro}} > 99\%$). The obtained results could be useful for design of the circular electrodes and effective suppression of their dendrites to avoid short-circuit.

ACKNOWLEDGMENTS

The authors gratefully acknowledge the financial support from Indian Institute of Technology Kharagpur [Sanction Letter No.: IIT/SRIC/ATDC/CEM/2013 – 14/118, dated 19.12.2013].

AUTHOR DECLARATIONS

Conflict of Interest

The authors have no conflicts to disclose.

Author Contributions

Trina Dhara contributed equally to this work.

Asghar Aryanfar: Conceptualization (equal); Data curation (equal); Formal analysis (equal); Investigation (equal); Software (equal); Validation (equal); Visualization (equal); Writing – original draft (equal); Writing – review & editing (equal). **Trina Dhara:** Data

curation (equal); Investigation (equal); Resources (equal); Writing – review & editing (equal). **Sunando DasGupta:** Funding acquisition (equal); Project administration (equal); Supervision (equal).

DATA AVAILABILITY

The raw data for producing the results in this manuscript are freely available upon request from the corresponding author at aryanfar@caltech.edu.

NOMENCLATURE

A_B	Bulk surface area (m^2)
A_S	Peripheral surface area (m^2)
a_1, a_2	Curve fitting coefficients
$\bar{b}$	Average thickness of electrodeposits (m)
C_0	Bulk electrolyte concentration (M)
D	Bulk diffusion coefficient ($m^2\ s^{-1}$)
D_{INT}	Interfacial diffusion coefficient ($m^2 s^{-1}$)
d_O/R_O	Dia./radius of the anode (m)
d_I/R_I	Dia./radius of the cathode (m)
E	Electric field (V/m^{-1})
F	Faraday's constant ($C\ mol^{-1}$)
$f(s)$	Augmentation ratio
f_{FIT}	Fitting function
f_1, f_2, f_3	Red/green/blue coefficients ([])
Int/Int_c	Intensity/critical intensity value
I, I_B, I_S	Total/bulk/surface current (A)
J	Binarized image
N	Number of pixels/microstructure
N_p	Number of pixels in the periphery
N_{CVX}	Number of points/convex hull
n	Valence number
q	Charge per volume ($C\ m^{-3}$)
$\bar{r}$	Normalized average radius
$\tilde{r}$	Normalized effective radius
$\hat{r}$	Normalized reach
s	Transient position/ growing front (m)
s_{min}	Position of minimum voltage (m)
t_k	Times in the step k
V_0	Applied voltage (V)
V_I, V_O	Voltage at inner/outer electrodes (V)
$V(R_O)$	Voltage at radius R_O (V)
v	Velocity of the front ($m\ s^{-1}$)
x, y	Horizontal/vertical coordinates
x_C, y_C	Horizontal/vertical coordinates of center
x_{CVX}	Horizontal coordinate/convex hull
y_{CVX}	Vertical coordinate/convex hull
β	Scaling factor ($mm\ pixel^{-1}$)
$\hat{v}_{\mathrm{INT}}$	Interpolated normalized velocity (s^{-1})
$\hat{v}_{min}$	Normalized minimum voltage
$\sigma^2, \sigma_0^2, \sigma_1^2$	Total/white/black pixels variance
$\phi_{\mathrm{Macro}}, \phi_{\mathrm{Micro}}$	Total/ macro-/micro-scale porosity
ω_0, ω_1	Fractions of while/black portions

REFERENCES

[1]J. Shalf, "The future of computing beyond Moores law," Phil. Trans. R. Soc. A **378**(2166), 20190061 (2020).
[2]J. Tollefson, "Charging up the future: A new generation of lithium-ion batteries, coupled with rising oil prices and the need to address climate change, has sparked a global race to electrify transportation," Nature **456**(7221), 436–441 (2008).
[3]S. F. J. Flipsen, "Power sources compared: The ultimate truth?," J. Power Sources **162**(2), 927–934 (2006).
[4]G. Crabtree, E. Kócs, and L. Trahey, "The energy-storage frontier: Lithium-ion batteries and beyond," MRS Bull. **40**(12), 1067–1078 (2015).
[5]P. J. Hall and E. J. Bain, "Energy-storage technologies and electricity generation," Energy Policy **36**(12), 4352–4355 (2008).
[6]M. Keyser, A. Pesaran, Q. Li, S. Santhanagopalan, K. Smith, E. Wood, S. Ahmed, I. Bloom, E. Dufek, M. Shirk *et al.*, "Enabling fast charging–battery thermal considerations," J. Power Sources **367**, 228–236 (2017).
[7]S. Ahmed, I. Bloom, A. N. Jansen, T. Tanim, E. J. Dufek, A. Pesaran, A. Burnham, R. B. Carlson, F. Dias, K. Hardy *et al.*, "Enabling fast charging–a battery technology gap assessment," J. Power Sources **367**, 250–262 (2017).
[8]J. M. Tarascon and M. Armand, "Issues and challenges facing rechargeable lithium batteries," Nature **414**(6861), 359–367 (2001).
[9]S-e Sheng, L. Sheng, L. Wang, N. Piao, and X. He, "Thickness variation of lithium metal anode with cycling," J. Power Sources **476**, 228749 (2020).
[10]K. Amine, I. Belharouak, Z. Chen, T. Tran, H. Yumoto, N. Ota, S.-T. Myung, and Y.-K. Sun, "Nanostructured anode material for high-power battery system in electric vehicles," Adv. Mater. **22**(28), 3052–3057 (2010).
[11]M. Kaliaperumal, M. S. Dharanendrakumar, S. Prasanna, K. V. Abhishek, R. K. Chidambaram, S. Adams, K. Zaghib, and M. V. Reddy, "Cause and mitigation of lithium-ion battery failure: A review," Materials **14**(19), 5676 (2021).
[12]M. Balaish, A. Kraytsberg, and Y. Ein-Eli, "A critical review on lithium–air battery electrolytes," Phys. Chem. Chem. Phys. **16**(7), 2801–2822 (2014).
[13]K. I. Popov, S. S. Djokić, N. D. Nikolić, and V. D. Jović, *Morphology of Electrochemically and Chemically Deposited Metals* (Springer, 2016).
[14]W. Giurlani, G. Zangari, F. Gambinossi, M. Passaponti, E. Salvietti, F. Di Benedetto, S. Caporali, and M. Innocenti, "Electroplating for decorative applications: Recent trends in research and development," Coatings **8**(8), 260 (2018).
[15]J. Liu, X. Fang, C. Zhu, X. Xing, G. Cui, and Z. Li, "Fabrication of superhydrophobic coatings for corrosion protection by electrodeposition: A comprehensive review," Colloids Surf., A **607**, 125498 (2020).
[16]I. Gurrappa and L. Binder, "Electrodeposition of nanostructured coatings and their characterization a review," Sci. Technol. Adv. Mater. **9**, 043001 (2008).
[17]S. Khorsand, K. Raeissi, and F. Ashrafizadeh, "Corrosion resistance and long-term durability of super-hydrophobic nickel film prepared by electrodeposition process," Appl. Surf. Sci. **305**, 498–505 (2014).
[18]G. Zhang, S. Sun, M. N. Banis, R. Li, M. Cai, and X. Sun, "Morphology-controlled green synthesis of single crystalline silver dendrites, dendritic flowers, and rods, and their growth mechanism," Cryst. Growth Des. **11**(6), 2493–2499 (2011).
[19]H. Yan, P. J. Boden, S. J. Harris, and J. Downes, "Morphology and fine structure of zinc electrodeposits," Philos. Mag. A **70**(2), 391–404 (1994).
[20]Y. Ren, Y. Shen, Y. Lin, and C.-W. Nan, "Direct observation of lithium dendrites inside garnet-type lithium-ion solid electrolyte," Electrochem. Commun. **57**, 27–30 (2015).
[21]R. Younesi, G. M. Veith, P. Johansson, K. Edström, and T. Vegge, "Lithium salts for advanced lithium batteries: Li-metal, li-o 2, and li-s," Energy Environ. Sci. **8**(7), 1905–1922 (2015).
[22]X. Ye, W. Xiong, T. Huang, X. Li, Y. Lei, Y. Li, X. Ren, J. Liang, X. Ouyang, Q. Zhang *et al.*, "A blended gel polymer electrolyte for dendrite-free lithium metal batteries," Appl. Surf. Sci. **569**, 150899 (2021).
[23]J. Steiger, D. Kramer, and R. Monig, "Mechanisms of dendritic growth investigated by in situ light microscopy during electrodeposition and dissolution of lithium," J. Power Sources **261**, 112–119 (2014).
[24]H. Liu, X.-B. Cheng, J.-Q. Huang, H. Yuan, Y. Lu, C. Yan, G.-L. Zhu, R. Xu, C.-Z. Zhao, L.-P. Hou *et al.*, "Controlling dendrite growth in solid-state electrolytes," ACS Energy Lett. **5**(3), 833–843 (2020).
[25]C.-Z. Zhao, H. Duan, J.-Q. Huang, J. Zhang, Q. Zhang, Y.-G. Guo, and L.-J. Wan, "Designing solid-state interfaces on lithium-metal anodes: A review," Sci. China Chem. **62**, 1286–1299 (2019).
[26]T. Foroozan, F. A. Soto, V. Yurkiv, S. Sharifi-Asl, R. Deivanayagam, Z. Huang, R. Rojaee, F. Mashayek, P. B. Balbuena, and R. Shahbazian-Yassar, "Synergistic effect of graphene oxide for impeding the dendritic plating of li," Adv. Funct. Mater. **28**(15), 1705917 (2018).

[27]K. Shen, Z. Wang, X. Bi, Y. Ying, D. Zhang, C. Jin, G. Hou, H. Cao, L. Wu, and G. Zheng, "Magnetic field–suppressed lithium dendrite growth for stable lithium-metal batteries," Adv. Energy Mater. **9**(20), 1900260 (2019).
[28]M. Ishikawa, S-i Machino, and M. Morita, "Electrochemical control of a li metal anode interface: Improvement of li cyclability by inorganic additives compatible with electrolytes," J. Electroanal. Chem. **473**(1–2), 279–284 (1999).
[29]A. Aryanfar, D. J. Brooks, A. J. Colussi, B. V. Merinov, W. A. Goddard III, and M. R. Hoffmann, "Thermal relaxation of lithium dendrites," Phys. Chem. Chem. Phys. **17**(12), 8000–8005 (2015).
[30]A. Aryanfar, T. Cheng, A. J. Colussi, B. V. Merinov, W. A. Goddard III, and M. R. Hoffmann, "Annealing kinetics of electrodeposited lithium dendrites," J. Chem. Phys. **143**(13), 134701 (2015).
[31]F. Ding, W. Xu, G. L. Graff, J. Zhang, M. L. Sushko, X. Chen, Y. Shao, M. H. Engelhard, Z. Nie, and J. Xiao, "Dendrite-free lithium deposition via self-healing electrostatic shield mechanism," J. Am. Chem. Soc. **135**(11), 4450–4456 (2013).
[32]M. Chen, M. Shao, J. Jin, L. Cui, H. Tu, and X. Fu, "Configurational and structural design of separators toward shuttling-free and dendrite-free lithium-sulfur batteries: A review," Energy Storage Mater. **47**, 629 (2022).
[33]W. Zhou, M. Chen, Q. Tian, J. Chen, X. Xu, and C.-P. Wong, "Cotton-derived cellulose film as a dendrite-inhibiting separator to stabilize the zinc metal anode of aqueous zinc ion batteries," Energy Storage Mater. **44**, 57–65 (2022).
[34]S. Choudhury, D. Vu, A. Warren, M. D. Tikekar, Z. Tu, and L. A. Archer, "Confining electrodeposition of metals in structured electrolytes," Proc. Natl. Acad. Sci. USA **115**(26), 6620–6625 (2018).
[35]Q. Li, S. Zhu, and Y. Lu, "3D porous cu current collector/li-metal composite anode for stable lithium-metal batteries," Adv. Funct. Mater. **27**(18), 1606422 (2017).
[36]Y. Liu, "Overview of the recent progress of suppressing the dendritic growth on lithium metal anode for rechargeable batteries," J. Phys.: Conf. Ser. **2152**, 012060 (2022).
[37]J. N. Chazalviel, "Electrochemical aspects of the generation of ramified metallic electrodeposits," Phys. Rev. A **42**(12), 7355–7367 (1990).
[38]C. Monroe and J. Newman, "Dendrite growth in lithium/polymer systems—A propagation model for liquid electrolytes under galvanostatic conditions," J. Electrochem. Soc. **150**(10), A1377–A1384 (2003).
[39]T. A. Witten and L. M. Sander, "Diffusion-limited aggregation," Phys. Rev. B **27**(9), 5686 (1983).
[40]V. Fleury, M. Rosso, and J. N. Chazalviel, "Geometrical aspect of electrodeposition - the Hecker effect," Phys. Rev. A **43**(12), 6908–6916 (1991).
[41]V. Fleury, J.-N. Chazalviel, M. Rosso, and B. Sapoval, "The role of the anions in the growth speed of fractal electrodeposits," J. Electroanal. Chem. Interfacial Electrochem. **290**(1–2), 249–255 (1990).
[42]V. Fleury, J.-N. Chazalviel, and M. Rosso, "Coupling of drift, diffusion, and electroconvection, in the vicinity of growing electrodeposits," Phys. Rev. E **48**(2), 1279 (1993).
[43]V. Fleury, "Branched fractal patterns in non-equilibrium electrochemical deposition from oscillatory nucleation and growth," Nature **390**(6656), 145–148 (1997).
[44]A. Jana, D. R. Ely, and R. E. García, "Dendrite-separator interactions in lithium-based batteries," J. Power Sources **275**, 912–921 (2015).
[45]Y. Ren, Y. Zhou, and Y. Cao, "Inhibit of lithium dendrite growth in solid composite electrolyte by phase-field modeling," J. Phys. Chem. C **124**(23), 12195–12204 (2020).
[46]P. P. Natsiavas, K. Weinberg, D. Rosato, and M. Ortiz, "Effect of prestress on the stability of electrode–electrolyte interfaces during charging in lithium batteries," J. Mech. Phys. Solids **95**, 92–111 (2016).
[47]C. P. Nielsen and H. Bruus, "Morphological instability during steady electrodeposition at overlimiting currents," Phys. Rev. E **92**(5), 052310 (2015).
[48]D. Barkey, "Morphology selection and the concentration boundary layer in electrochemical deposition," J. Electrochem. Soc. **138**(10), 2912 (1991).
[49]D. Barkey, P. Garik, E. Ben-Jacob, B. Miller, and B. Orr, "Growth velocity, the limiting current, and morphology selection in electrodeposition of branched aggregates," J. Electrochem. Soc. **139**(4), 1044 (1992).
[50]C.-P. Chen and J. Jorné, "Fractal analysis of zinc electrodeposition," J. Electrochem. Soc. **137**(7), 2047 (1990).
[51]N. M. Santos and D. M. F. Santos, "A fractal dimension minimum in electrodeposited copper dendritic patterns," Chaos, Solitons Fractals **116**, 381–385 (2018).
[52]D. Grier, E. Ben-Jacob, R. Clarke, and L.-M. _. Sander, "Morphology and microstructure in electrochemical deposition of zinc," Phys. Rev. Lett. **56**(12), 1264 (1986).
[53]M. Matsushita, M. Sano, Y. Hayakawa, H. Honjo, and Y. Sawada, "Fractal structures of zinc metal leaves grown by electrodeposition," Phys. Rev. Lett. **53**(3), 286 (1984).
[54]D. B. Hibbert and J. R. Melrose, "Electrodeposition in support: Concentration gradients, an ohmic model and the genesis of branching fractals," Proc. R. Soc. London A. Math. Phys. Sci. **423**(1864), 149–158 (1989).
[55]D. G. Grier, D. A. Kessler, and L. M. Sander, "Stability of the dense radial morphology in diffusive pattern formation," Phys. Rev. Lett. **59**(20), 2315 (1987).
[56]M. Qiu, G. D. Finlayson, and G. Qiu, "Contrast maximizing and brightness preserving color to grayscale image conversion," In *Conference on Colour in Graphics, Imaging, and Vision* (Society for Imaging Science and Technology, 2008), Vol. 2008, pp. 347–351.
[57]N. Otsu, "A threshold selection method from gray-level histograms," IEEE Trans. SMC. **9**(1), 62–66 (1979).
[58]A. Aryanfar, M. R. Hoffmann, and W. A. Goddard III, "Finite-pulse waves for efficient suppression of evolving mesoscale dendrites in rechargeable batteries," Phys. Rev. E **100**(4), 042801 (2019).
[59]D. Bradley and G. Roth, "Adaptive thresholding using the integral image," J. Graphics Tools **12**(2), 13–21 (2007).
[60]A. J. Bard and L. R. Faulkner, *Electrochemical Methods: Fundamentals and Applications* (Wiley, New York, 1980), Vol. 2.
[61]R. A. Noulty and D. G. Leaist, "Diffusion in aqueous copper sulfate and copper sulfate-sulfuric acid solutions," J. Solution Chem. **16**(10), 813–825 (1987).
[62]A. Aryanfar, A. Tayyar, and W. A. Goddard III, "Dendritic propagation on circular electrodes: The impact of curvature on the packing density," Phys. Rev. E **108**(1), 014801 (2023).